Discover Oncology

Research

An energy metabolism-related signature relevant to the tumor immune microenvironment in HNSCC

Kaiyu Zhu[1,2,3] · Yang Bai[3,4] · Changwei Lin[3] · Guilin Song[1] · Yifei Chen[1]

Received: 25 November 2024 / Accepted: 9 May 2025

Abstract

The importance of energy metabolism in cancer was explored by accumulating studies. Energy metabolism can affect the cellular activities of tumors. However, there is few research exploring the role of energy metabolism in tumor immune microenvironment. In this context, we constructed a novel energy metabolism-related prognostic signature containing 8 genes. The risk score calculated by the signature was analyzed to be an independent value of head and neck squamous cell carcinoma (HNSCC). We further validated the effectiveness and accuracy of our signature in The Cancer Genome Atlas Program (TCGA) cohort and Gene Expression Omnibus (GEO) cohort. Moreover, we also revealed a negative correlation between the risk score and the activity of the immune processes. Finally, we validated the function of *Desmoglein 2 protein (DSG2)*, a risk gene in the signature, in tumor progression and found that knockdown of *DSG2* remarkably suppressed the proliferation and migration of HNSCC cells, which further validated our analysis. In conclusion, the energy metabolism-related gene signature we built is a prospective biomarker of HNSCC, which can offer valuable clues for the research and development of immunotherapeutic drugs in HNSCC.

Keywords Energy metabolism · Head and neck squamous cell carcinoma · Prognostic signature · Tumor immune microenvironment · *DSG2*

Abbreviations

ACADL	Acyl-CoA dehydrogenase long chain
APP	Amyloid-β precursor protein
AUC	Area under the curve
CCK-8	Cell Counting Kit-8
CDKN2 A	Cyclin-dependent kinase inhibitor 2A
DEG	Differentially expressed gene
DSG2	Desmoglein 2

Kaiyu Zhu and Yang Bai are co-first authors on this work.

Supplementary Information The online version contains supplementary material available at https://doi.org/10.1007/s12672-025-02652-7.

✉ Yifei Chen, yifeichenfiona@126.com | [1]Department of Otolaryngology Head Neck Surgery, The Fourth Hospital of Changsha (Integrated Traditional Chinese and Western Medicine Hospital of Changsha, Changsha Hospital of Hunan Normal University), 200 Jinxing North Road, Changsha 410219, Hunan, People's Republic of China. [2]Center for Gastrointestinal Surgery, The First Affiliated Hospital, Sun Yat-Sen University, Guangzhou 510080, People's Republic of China. [3]Department of Gastrointestinal Surgery, The Third Xiangya Hospital of Central South University, Changsha 410013, Hunan, People's Republic of China. [4]Postdoctoral Station of Basic Medicine, The Third Xiangya Hospital, Central South University, Changsha 410013, Hunan, People's Republic of China.

ECM	Extracellular matrix
EMRDEG	Energy metabolism–related differentially expressed gene
EMRG	Energy metabolism–related gene
EMT	Epithelial-mesenchymal transition
FBS	Fetal bovine serum
FC	Fold-change
FDR	False discovery rate
GAPDH	Glyceraldehyde-3-phosphate dehydrogenase
GEO	Gene Expression Omnibus
GRIA3	Glutamate ionotropic receptor AMPA type subunit 3
GSEA	Gene set enrichment analysis
HNSCC	Head and neck squamous cell carcinoma
HPA	Human Protein Atlas
IQCN	IQ motif containing N
KEGG	Kyoto Encyclopedia of Genes and Genomes
LASSO	Least absolute shrinkage and selection operator
NK	Natural killer
OS	Overall survival
PEMRDEG	Prognostic energy metabolism-related differentially expressed gene
qRT-PCR	Quantitative real-time reverse transcriptase-polymerase chain reaction
ROC	Receiver operating characteristic
shDSG2	DSG2-specific shRNA
shNC	Negative control shRNA
SYT1	Synaptotagmin 1
TCGA	The Cancer Genome Atlas
TIIC	Tumor-infiltrating immune cell
TIME	Tumor microenvironment
TIMER	Tumor Immune Estimation Resource
TMC8	Transmembrane channel like 8
TNF	Tumor necrosis factor
TNFRSF4	TNF receptor superfamily member 4
UCSC	University of California, Santa Cruz
uni-Cox	Univariate Cox regression

1 Introduction

HNSCC is a series of heterogeneous epithelial tumors that develop in the upper aerodigestive tract [1], occurring mostly in the larynx (supraglottic, glottis, and infraglottic), oral cavity (tongue, floor of the mouth, hard palate, buccal mucosa, and alveolar ridge), and oropharynx (lateral pharyngeal wall, posterior pharyngeal wall, tongue root, tonsils, and soft palate) [2]. As one of the most frequent cancer types worldwide, HNSCC is inevitably a major cause of cancer-related poor prognosis; for instance, an estimated 878,348 new cases of and 444,347 deaths due to HNSCC were reported in 2020. Treatment outcomes among patients with HNSCC have improved due to the development of surgical and radiation techniques [1] and multimodal therapeutic approaches including targeted therapy and immunotherapy [3]. However, challenges remain in individualized treatment and the prognosis of HNSCC owing to its high mutation rate, locally advanced or recurrent/metastatic (R/M) status, and major changes in the clinical characteristics of patients with HNSCC. Hence, novel targets for HNSCC prognosis prediction and treatment are urgently needed.

Metabolic reprogramming is a fundamental trait of most cancer types [4]. As a core metabolic process, the integration of energy metabolism involves the effect of hormones on metabolic pathways by affecting individual physiological processes [5]. For instance, Peng et al. [6] identified tumor subtypes in 33 cancers on the basis of seven metabolic processes including the integration of energy metabolism, also showing that the integration of energy metabolism might be a significant factor affecting the survival and prognosis among patients with HNSCC. However, this study does not focus on the integration of energy metabolism or delve into its effects in HNSCC; hence, future studies are required to investigate whether integration of energy metabolism-related genes qualify as targets to assess the prognosis and treatment of HNSCC.

The tumor immune microenvironment (TIME) plays a critical role in cancer progression and is markedly involved in HNSCC advancement by maintaining the survival of tumor cells [7]. For instance, a previous study reported that the competitive metabolic effects of cancer cells on glucose could inhibit the differentiation and proliferation of tumor-infiltrating T lymphocytes by regulating nutrient absorption in the TIME [8]. However, it remains unknown whether and what role does the integration of energy metabolism play in the TIME in HNSCC. Herein, we collected HNSCC mRNA transcriptome profiling data from TCGA and classified the differentially expressed mRNAs associated with the integration of energy metabolism. Thereafter, a prognostic signature was developed, and further analyses focused on the TIME. This study aimed to generate a novel prognostic model for HNSCC and present a promising direction for further exploration of immunotherapy for HNSCC.

2 Materials and methods

2.1 Data collection

RNA-seq data of 546 HNSCC samples (502 tumor samples and 44 healthy samples) were acquired from TCGA (https://portal.gdc.cancer.gov/projects/TCGA-HNSC) [9]. The gene symbol was annotated by GENCODE Human Release 36. The corresponding clinical information was obtained from the UCSC (University of California, Santa Cruz) Xena genome browser (https://xenabrowser.net/datapages/) [10]. Expression profiling data in the form of fragments per kilobase of million mapped reads were converted to trans per million and then log2-normalized. The GEO (Gene Expression Omnibus) cohort comprised the GSE41613 (97 samples) [11] and GSE10300 (44 samples) [12] data sets (https://www.ncbi.nlm.nih.gov/geo/). Before merging the expression matrices of the GEO cohorts, we removed batch effects using the “limma” package in R (The R Foundation). Data regarding the integration of energy metabolism (comprising 110 genes; listed in Table S1) were downloaded from an article published in Cell Reports [6].

2.2 Screening of energy metabolism–related differentially expressed genes

The “limma” package in R [13] was used to screen differentially expressed genes between 502 tumor samples and 44 normal samples ($|\log2 \text{ fold-change [FC]}| > 1$, false discovery rate [FDR] < 0.05). Spearman correlation and intersection analyses were conducted to screen energy metabolism–related differentially expressed genes (EMRDEGs). Thereafter, univariate Cox regression (uni-Cox) analysis was carried out to identify the candidate genes significantly associated with overall survival (OS) among patients with HNSCC by analyzing EMRDEGs using the “survival” package in R ($P < 0.05$).

2.3 Construction of the prognostic signature

Least absolute shrinkage and selection operator (LASSO) regression analysis was performed to generate a prognostic signature based on the training group with follow-up information and data regarding the expression levels of prognostic EMRDEGs. We finally identified an 8-gene prognostic signature, whose risk score was computed using the following formula:

$$Risk\ score = \sum\nolimits_{1}^{n} coef_{i} \times x_{i}$$

In the aforementioned equation, i, n, x_i, and [coef]_i represent the selected gene, total number of genes, expression value of the gene, and corresponding coefficient values, respectively.

2.4 Assessment and verification of the prognostic model

Independent prognostic analysis was carried out to investigate whether the risk score and clinical characteristics were independent prognostic indices for patients with HNSCC on uni- and multivariate Cox analyses. The nomogram was plotted to predict the survival rate using the "rms" package in R. Subsequently, the predictive ability of the nomogram was assessed using a calibration curve. Kaplan–Meier analysis was carried out to determine the difference in overall survival (OS) between the distinct groups. The time-dependent receiver operating characteristic (ROC) [14] curve was plotted to estimate the prognostic specificity and sensitivity of the prognostic signature.

2.5 Gene set enrichment analysis

Gene set enrichment analysis (GSEA) can reveal related metabolic pathways and processes, which allows focusing on the gene set rather than high-scoring genes. Using the "clusterProfiler" R package [15], GSEA was conducted to detect differences in molecular mechanisms and functions between the two risk groups. KEGG (Kyoto Encyclopedia of Genes and Genomes) and hallmark gene sets were acquired from MSigDB (https://www.gsea-msigdb.org/gsea/) [16] (listed in Table S2).

2.6 Tumor immune microenvironment analysis

The ESTIMATE algorithm was used to determine the stromal scores, immune scores, and ESTIMATE scores to evaluate the infiltration of stromal and immune cells in patients with HNSCC [17]. The abundance of the 22 tumor-infiltrating cells in the two risk groups was assessed to elucidate the TIME in HNSCC using the CIBERSORT algorithm (http://CIBERSORT.stanford.edu/) [18]. The Tumor Immune Estimation Resource (TIMER) website (http://timer.cistrome.org/) [19] was used to further detect the influence of the signature on the infiltration abundance of classical immune cells (B, CD4+ T, and CD8+ T lymphocytes; macrophages; neutrophils; and myeloid dendritic cells).

2.7 Analysis of sensitivity to immunotherapy and pharmacotherapy

TIDE (http://tide.dfci.harvard.edu/) [20] was performed to assess the responses to anti- cytotoxic T-lymphocyte associated protein 4 and anti–programmed cell death protein 1 immunotherapy. To predict the half inhibitory concentration levels of anticancer drugs, the "pRRophetic" package in R [21] was used.

2.8 Ethics approval statement

All procedures in our study involving human tissues and animals adhered to the ethical standards set by the Institutional Ethics Committee of The Fourth Hospital of Changsha, as well as the 1964 Helsinki Declaration and its subsequent amendments. The study was approved by the Institutional Ethics Committee of The Fourth Hospital of Changsha (No. CSSDSYY-YXLL-SC-2023-03-03 and No. CSSDSYY-YXLL-SC-2023-03-163). Written informed consent was obtained from all patients. All methods were carried out in accordance with relevant guidelines and regulations.

2.9 RNA extraction and quantitative real-time reverse transcriptase polymerase chain reaction

Total RNA from tissues was extracted using the Total RNA Extraction Reagent kit (10606ES60, Yeasen, Shanghai, China) in accordance with the manufacturer's instructions. Reverse transcription was carried out using the obtained RNAs, using a cDNA synthesis kit (10606ES60, Yeasen). Gene expression was quantified using a Roche LightCycler 480 machine using SYBR Green Master Mix (11201ES03, Yeasen), using the $2^{-\Delta\Delta Ct}$ method with *GAPDH (glyceraldehyde-3-phosphate dehydrogenase)* as the internal reference for normalization. The mean Ct value of *DSG2* in normal tissues was designated as the calibrator, and the formula of the $2^{-\Delta\Delta Ct}$ method was as follows: $\Delta Ct(\text{sample}) = Ct(\text{gene}) - Ct(\text{GAPDH})$, $\Delta\Delta Ct(\text{sample}) = \Delta Ct(\text{sample}) - \Delta Ct(\text{calibrator})$. Additionally, all primers (Table S3) were synthesized by Tsingke Biotech (Tsingke, Beijing, China).

2.10 Cell lines and cell culture

The human pharyngeal squamous carcinoma cell line FADU was cultured in minimum essential medium (KeyGEN, BioTECH, Nanjing, China) containing 10% fetal bovine serum (FBS; Biological Industries, Beit HaEmek, Israel). The cells were cultured at 37 °C in a humidified atmosphere containing 5% CO_2.

2.11 Lentiviral vector construction and cell transfection

shRNA was constructed using plasmid plvx-shRNA1 (Clontech, catalog number 632177). To generate stable lentivirus-transduced lines, cells were infected with the lentivirus and polybrene in accordance with the manufacturer's recommendations, and stable cell lines were selected with 4 μg/mL of puromycin treatment after 72 h of transfection. The efficiency in different cells was determined via quantitative real-time reverse transcriptase–polymerase chain reaction (qRT-PCR). The shRNA sequences are as follows: *sh-DSG#1*, GCTCAAACTAACGAAGGAATT; and *sh-DSG2#2*, GCTCAAGTTCAGATTCGTATT. The loss of *DSG2* expression was validated by qRT-PCR with primers: forward, CTAACA GGTTACGCTTTGGATGC; and reverse, GTGAACACTGGTTCGTTGTCAT.

2.12 Cell counting Kit-8 assay

Cells were seeded (5000/well) and cultured in 96-well plates for 24 h. The Cell-Counting Kit-8 (CCK-8; 10:100) reagent was added into each well at 24, 48, 72, and 96 h after the cells were seeded, and the mixture was incubated at 37 °C for 2 h in the next 4 days. Relative cell proliferation was assessed on the basis of the absorbance (determined at 450 nm) of each well, determined using an EnVision microplate reader (PerkinElmer, Waltham, MA, United States).

2.13 Transwell migration/invasion assay

Cell invasion assays were performed by using the Transwell chamber (24 wells and membranes with 8.0-μm pores; Corning, Glendale, AZ, United States) coated with Matrigel (Corning). Approximately 2 × 105 cells were seeded in the upper chamber containing serum-free medium along with 0.5% bovine serum albumin. The lower chamber contained chemoattractant in medium infused with 10% FBS. After incubation for approximately 24–30 h and removal of the non-invading cells with PBS, the invading cells were fixed with formaldehyde and stained with 0.5% crystal violet for 30 min at room temperature. The images were captured using an inverted microscope system (IX73, Olympus, Tokyo, Japan).

2.14 Plate colony formation assay

Approximately 500 treated cells were seeded in 6-well plates in triplicates and cultured for 10–14 days. After washing with PBS, the colonies were fixed with 4% paraformaldehyde for 30 min and stained with 0.25% crystal violet for 15 min at 25 °C. Finally, the colonies were imaged and counted.

2.15 Tumor xenografts

All experimental procedures involving animals used in this study were approved by the Animal Ethics Committee of Central South University. Female BALB/c nude mice (aged 4–5 weeks, weighing 18–20 g), purchased from the Department of Laboratory Animals of Central South University, were maintained under specific pathogen-free conditions. Respectively, 5 × 106 FADU-*shNC* cells, FADU-*shDSG2#1* cells, and FADU-*shDSG2#2* cells were inoculated subcutaneously into the left armpit of the nude mice. The minimum width and maximum length of the tumor were measured using a caliper every 4 days. As stipulated by the Animal Committee, the maximum tumor size for mice should not exceed 2000 mm^3 within the mice body, meaning that the diameter of any dimension must be less than 20 mm. In our study, all implanted tumors in mice were maintained below the maximum permitted dimensions of 20 mm in diameter and 2000 mm^3 in volume.

After approximately 6–7 weeks, all the mice were euthanized by cervical dislocation, and all the organs were harvested for examination.

2.16 Statistical analysis

Statistical analysis was performed using R software (version 4.1.3). Correlations were assessed using Spearman's correlation analysis. Cox regression, LASSO, and Kaplan–Meier analyses were carried out for survival analysis. Continuous variables were tested using the Wilcoxon signed-rank test. The threshold for statistical significance was set at $P < 0.05$.

3 Results

3.1 Identification of EMRDEGs

The research flow chart of our study is shown in Fig. 1. Spearman correlation analysis was performed between the 110 genes (Table S1) from the integration of energy metabolism set and other 19,828 genes in the TCGA cohort to screen energy metabolism–related genes (EMRGs), for which, the inclusion parameters were $|r| > 0.6$ and $P < 0.001$—this yielded 4262 EMRGs. Subsequently, we used the "limma" package in R and screened out 3402 differentially expressed genes (DEGs) between tumor samples and normal samples ($\log_2|FC| > 1.0$ and $FDR < 0.05$), of which 1789 were upregulated and 1613 were downregulated DEGs in the TCGA-HNSCC samples. The results are visualized using a volcano map (Fig. 2A). A Venn plot was generated to visualize overlaps between EMRGs and DEGs—these ($n = 877$) were defined as EMRDEGs (Fig. 2B).

3.2 Establishment and assessment of the risk model

After excluding normal samples and those with missing follow-up information, 501 tumor samples containing the information regarding survival time and status were obtained for survival analysis. We performed uni-Cox analysis to assess the prognostic value of 877 EMRDEGs and identified 46 prognostic EMRDEGs (PEMRDEGs) correlated with OS (Fig. 2C). Eleven PEMRDEGs were considered "risk" genes, and the remaining 35 were considered "protective" genes. The correlation between the 46 PEMRDEGs and those associated with the integration of energy metabolism ($n = 110$) is shown in Fig. 2D. Thereafter, we categorized the TCGA-HNSCC samples ($n = 501$) into the training group ($n = 252$) and the internal validation group ($n = 249$) in a 1:1 ratio. Because of the small number of patients at the M1 stage in the TCGA-HNSCC data set ($n = 1$), we excluded M-stage HNSCC as a clinical feature. The training group with information regarding survival time, survival status, and expression data for 46 PEMRDEGs was involved in the subsequent generation of the prognostic signature. Detailed information regarding the clinical characteristics of the two groups is provided in Table 1.

LASSO analysis was carried out to establish the best EMRG signature in the training group (Fig. 3A, B). Thereafter, an 8-EMRG prognostic signature, which includes *(acyl-CoA dehydrogenase long chain) ACADL*, *(amyloid-β precursor protein) APP*, *DSG2*, *(glutamate ionotropic receptor AMPA type subunit 3) GRIA3*, *(IQ motif containing N) IQCN*, *(synaptotagmin 1) SYT1*, *(transmembrane channel like 8) TMC8*, and *(TNF [tumor necrosis family] receptor superfamily member 4) TNFRSF4* was weighed by LASSO-Cox regression coefficients and reached optimal regression efficiency. Each patient's risk score was calculated as follows:

$$\begin{aligned}\text{Risk score } &= ACADL \times 0.28093 + APP \times 0.24723 + DSG2 \times 0.04929 + GRIA3 \times (-0.27600)\\ &\quad + IQCN \times (-0.45747) + SYT1 \times 0.20927 + TMC8 \times (-0.13101) + TNFRSF4 \times (-0.09784)\end{aligned}$$

Among the 8 EMRGs, *ACADL*, *APP*, *DSG2*, and *SYT1* were considered risk genes while the remaining 4 were considered protective genes. To further investigate the value of our model, we divided patients in the TCGA-HNSCC data set into high- and low-risk groups in accordance with the median risk score.

To determine the independent predictive value of the 8-EMRG signature, we used both uni- and multivariate Cox regression analyses (Fig 3C, D). We found that the risk score (hazard ratio: 2.506) and age (hazard ratio: 1.413) had independent prognostic value. Based on the clinical characters of patients with HNSCC, we constructed a nomogram to predict the OS of patients with HNSCC by adding up the corresponding scores of the relevant factors (Fig. 3E). The

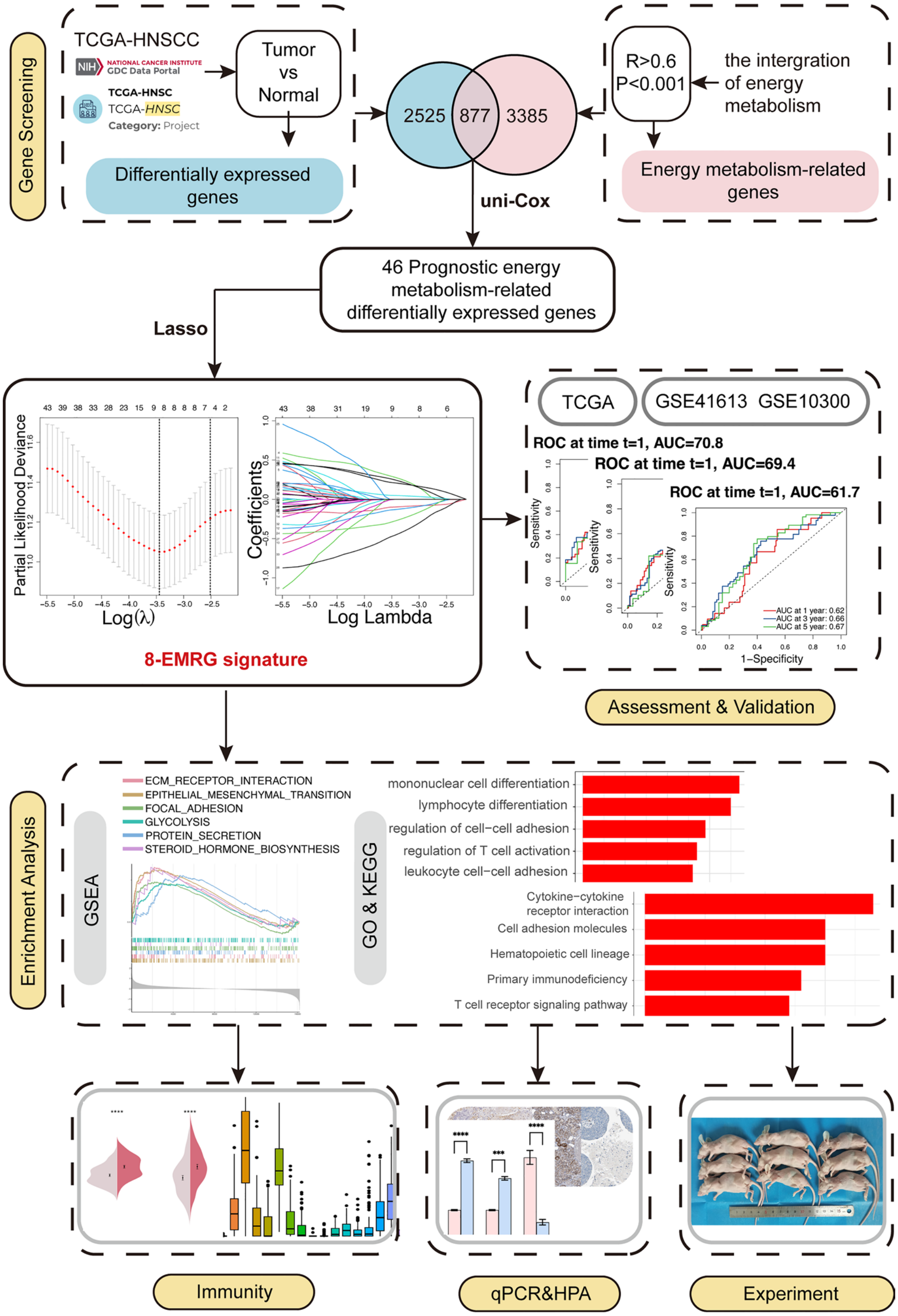

Fig. 1 Study flowchart. A total of 19,938 mRNAs and the integration of energy metabolism (110 genes) were obtained. Spearman correlation analysis was used to define 877 EMRDEGs. Then, forty-six prognostic EMRGs were identified by using uni-Cox regression analysis. A prognostic model with 8 prognostic EMRGs was constructed. Subsequently, GSEA analyses, immune-related analyses, somatic mutation, and drug sensitivity analysis were applied to identify the potential function of this signature. Finally, we performed qRT-PCR, CCK-8 assay, cell invasion assay, plate colony formation assay, and animal experiment to further validate our signature in vitro and in vivo

calibration plot was visualized to confirm that the result of the nomogram had a relatively high probability of being consistent with that of the prediction (Fig. 3F).

3.3 Validation of the 8-EMRG signature

We validated the prognostic signature in the TCGA cohort. The distributions of the risk score and the survival time in the two risk groups are shown in Fig. 4A, B, D, E, which suggested that the grouping based on the risk scores was random and reasonable. Moreover, Kaplan–Meier survival curves show that high-risk patients have a shorter OS (Fig. 4G, H). Furthermore, an ROC curve was plotted to better assess the prognostic precision of the signature. The high area

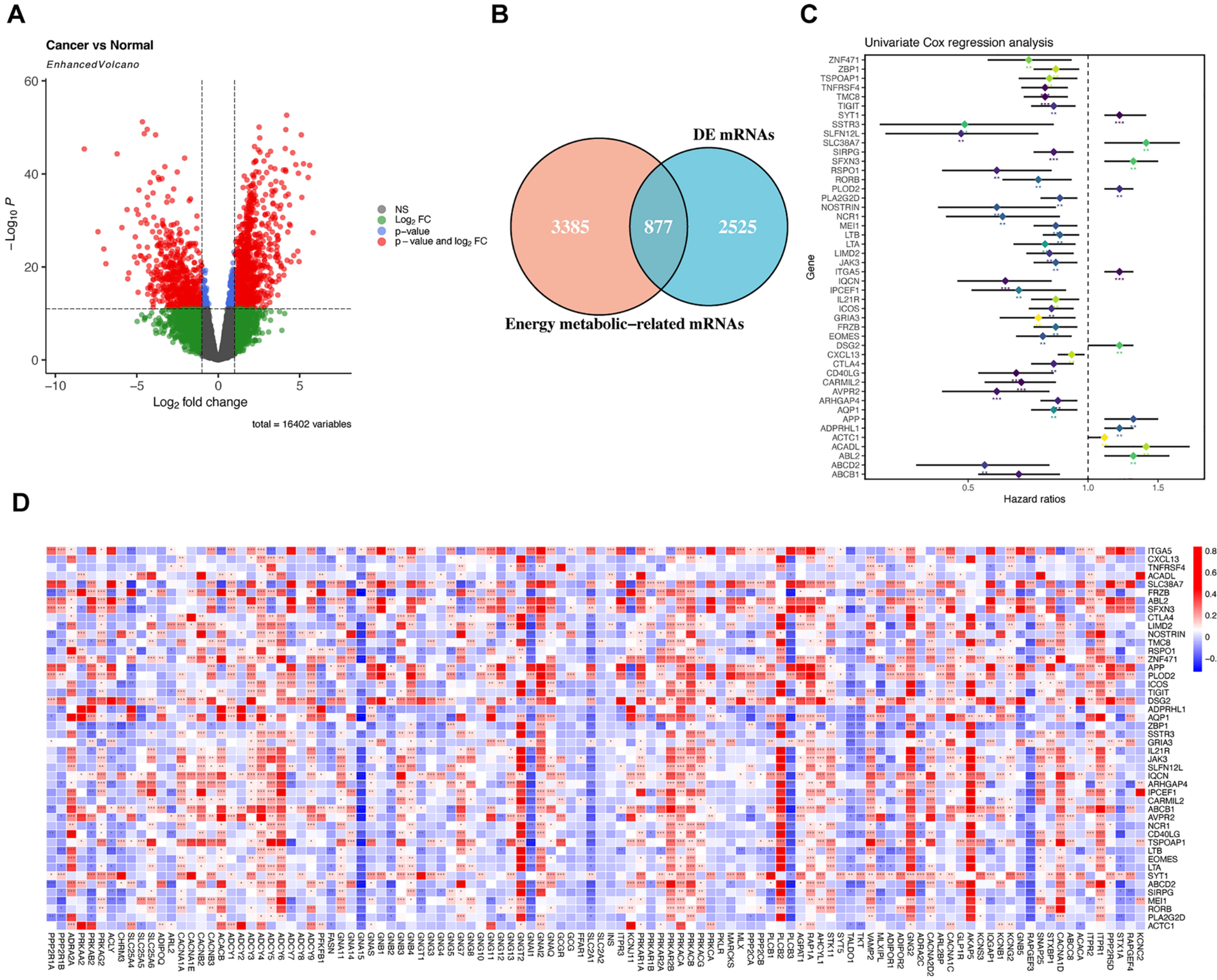

Fig. 2 Identification of DEGs and prognostic analysis of EMRDEGs: **A** the volcano plot of mRNAs. Green point indicates |log2 FC|> 1, blue point indicates FDR < 0.05, red point indicates |log2 FC|> 1 and FDR < 0.05. **B** Venn diagram to identify the common genes of DEGs and EMRGs. **C** Forest plot showed the results of the univariate Cox regression analysis of approximately 46 prognostic EMRDEGs. **D** The correlation between 46 prognostic EMRDEGs and 110 genes from the integration of energy metabolism

under the curve (AUC) values we obtained indicate that the signature has superior specificity and sensitivity in predicting OS among patients in the TCGA-HNSCC cohort (Fig. 4J, K). Thereafter, we validated the prognostic signature in the GEO cohort repeatedly to assess our model's ability to predict the survival of patients from other databases. After downloading the data and removing batch effects, we merged the gene expression matrices of the GSE10300 (44 samples) and GSE41613 (97 samples) data sets and divided these 141 patients into two risk groups to repeat the aforementioned analysis for patients registered in GEO data sets. The grouping of these patients also demonstrated randomization and rationality (Fig. 4C, F). We also observed a shorter OS in the high-risk group than in the low-risk group (Fig. 4I). The outstanding AUC values show that our signature had superior predictive performance (Fig. 4L).

In addition, the Kaplan–Meier curves for patients in the TCGA-HNSCC data set plotted on the basis of clinical characteristics consistently revealed that patients in the low-risk group had better survival outcomes than those in the high-risk group (Fig. 5A–J). These results show that the mortality rate of patients with HNSCC is positively correlated with the risk score computed by our risk model.

Table 1 The clinical characteristics of HNSCC patients in the training and internal validation group

Characteristics	Training group no	Internal validation group no	P-value
Age	–	–	–
≤ 65	80	87	> 0.05
> 65	159	150	–
Gender	–	–	–
Male	177	171	> 0.05
Female	62	66	–
Stage	–	–	––
I	8	9	> 0.05
II	51	43	–
III	52	48	–
IV	128	137	–
T stage	–	–	–
T1	15	16	> 0.05
T2	69	68	––
T3	75	59	––
T4	80	94	––
N stage	–	––	–
N0	120	117	> 0.05
N1	45	35	–
N2	73	79	–
N3	1	6	–

3.4 GSEA, gene ontology, and KEGG analyses: identification of differences in molecular functions and pathways

To assess differences in biological pathways and functions between the two risk groups, GSEA was performed on the basis of based on the KEGG and hallmark gene sets (Table S2). Our results show that many pathways associated with cancer proliferation had high activity in patients in the high-risk group, such as extracellular matrix (ECM) receptor interaction and epithelial mesenchymal transition (Fig. 6A). Glycolysis—a pathway related to tumor energy metabolism—was also enriched, which indicated that energy metabolism may influence the metastasis and proliferation of tumor cells in HNSCC. Many immune-related pathways were activated in the low-risk group (Fig. 6B). Moreover, focal adhesion and ECM receptor interaction, which are related to drug resistance, were also activated in the low-risk group. Furthermore, Gene Ontology and KEGG analyses revealed that many immune-related processes and pathways were enriched in patients with HNSCC (Fig. 6C, D). Our results show that the prognostic signature had a strong relationship with tumor progression, energy metabolism, immune process and drug resistance in HNSCC.

3.5 Analysis of the tumor immune microenvironment in the 8-EMRG signature

According to the encouraging results obtained from previous enrichment analyses, we aimed to further explore the association between the 8-EMRG signature and the TIME. The scores potentially reflecting tumor and stromal cell infiltration were calculated using the ESTIMATE algorithm. We found that low-risk patients had higher scores in both cohorts, which was consistent with the results of GSEA (Fig. 7A, B). Moreover, we used CIBERSORT to determine the levels of immune cell infiltration in patients in the TCGA-HNSCC and GEO cohorts. The proportion of the 22 tumor-infiltrating immune cells (TIICs) was visualized using the "ggpubr" package in R (Fig. 7C, D). We also investigated differences in the infiltration of TIICs between different risk groups in the two cohorts, and outcomes revealed that native B lymphocytes, memory-activated CD4+ T lymphocytes, CD8+ T lymphocytes, follicular helper T lymphocytes, γδ T lymphocytes, M0 macrophages, resting natural killer (NK) cells, and activated NK were obviously distinct between the different risk groups in the TCGA and GEO cohorts (Fig. 7E,).

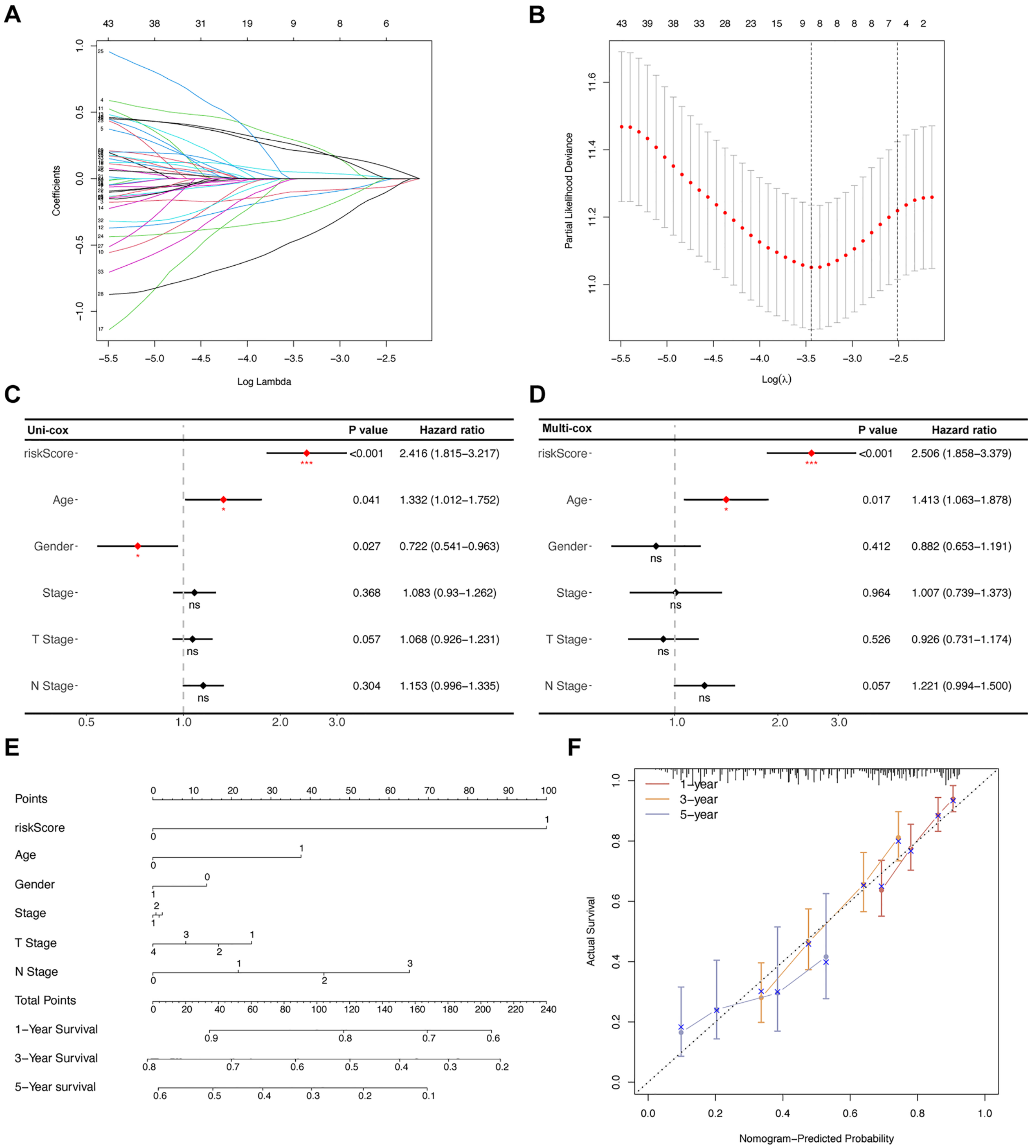

Fig. 3 Construction of an 8-EMRG signature and the analysis of independent prognostic potential: **A**, **B** The cvfit and lambda curves showing LASSO regression were performed with the minimum criteria. **C**, **D** The results of the univariate Cox analysis and multivariate Cox analysis of clinical factors and risk score with OS. *p < 0.05, **p < 0.01, ***p < 0.001. ns, No significance. **E** The nomogram to predict the 1-year, 3-year, and 5-year overall survival rates of TCGA-HNSCC patients. **F** The calibration plot for evaluating the accuracy of the nomogram model. The dashed diagonal line in gray represents the ideal nomogram

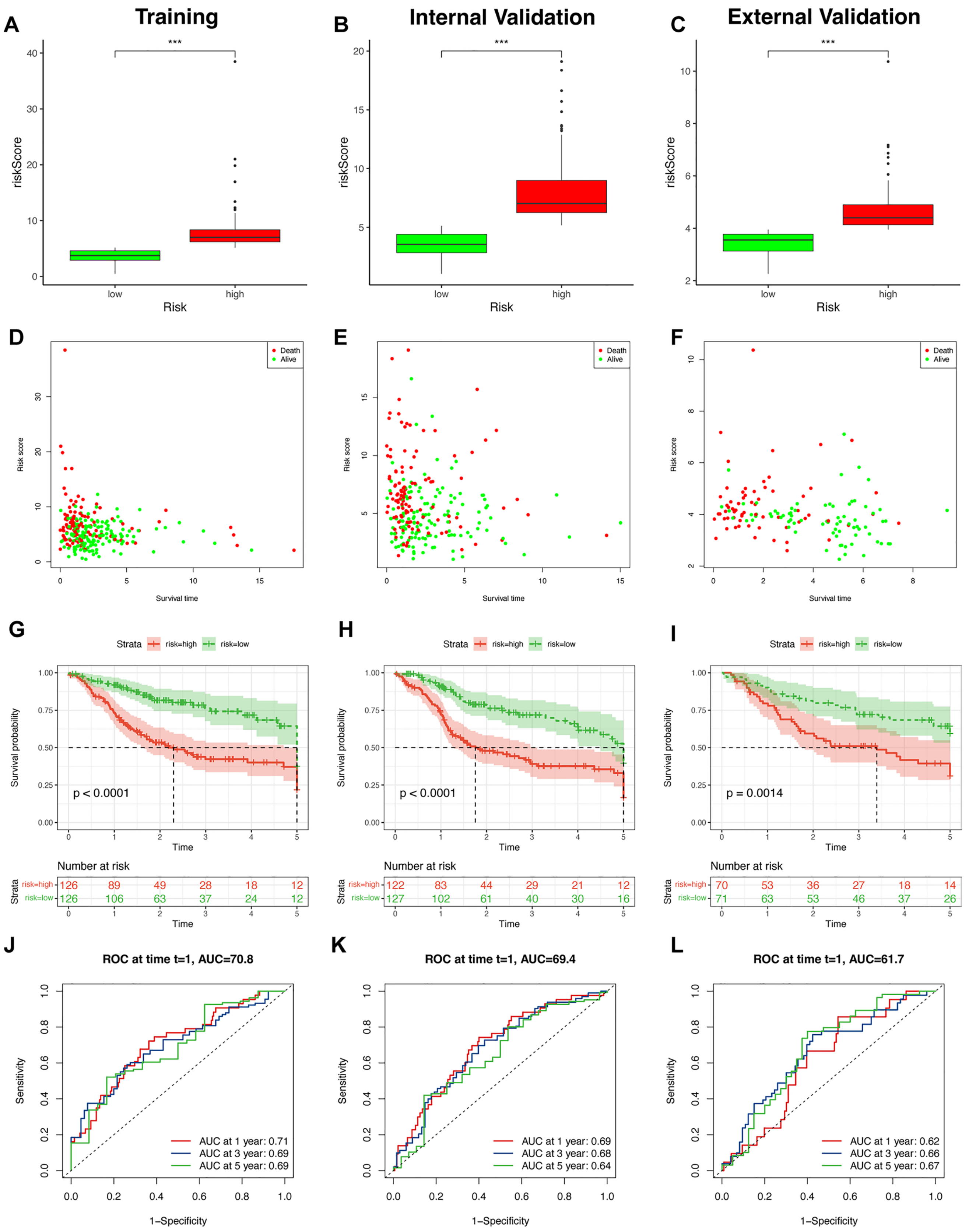

Fig. 4 Verification of the 8-EMRG signature model in the training, internal validation, and external validation groups: The distributions of the risk scores and overall survival status in the training (**A**, **D**), internal validation (**B**, **E**), and external validation (**C**, **F**) groups, *p < 0.05, **p < 0.01, and ***p < 0.001. Kaplan–Meier curves for survival status and survival time in the training (**G**), internal validation (**H**), and external validation (**I**) groups. The 1-year, 3-year, and 5-year ROC curves of the training (**J**), internal validation (**K**), and external validation (**L**) groups, respectively

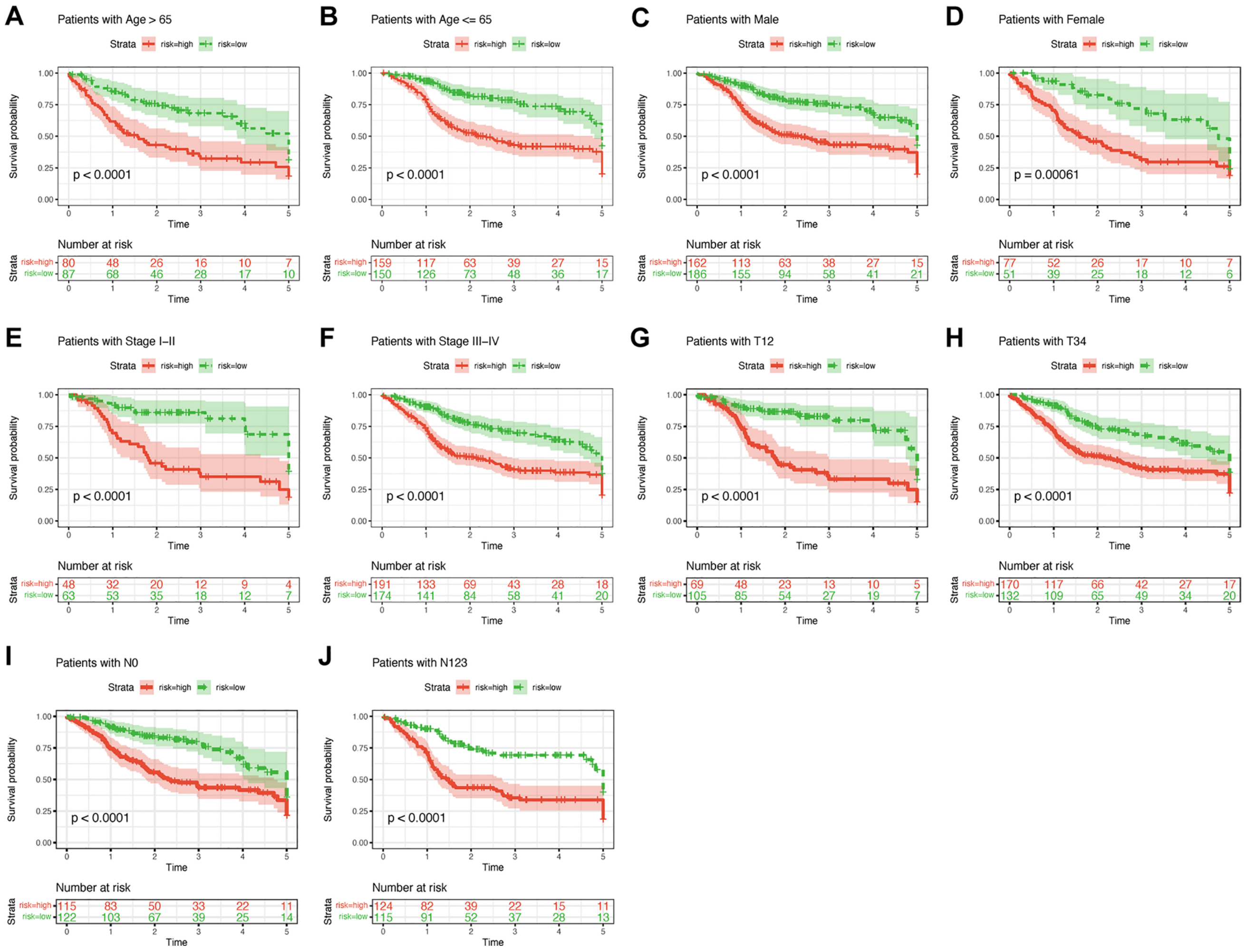

Fig. 5 The prognostic ability of the 8-EMRG signature for OS in multiple HNSCC subtypes. Kaplan–Meier curves for OS prediction in HNSCC subtypes of **A** age > 65 years, **B** age ≤ 65 years, **C** male, **D** female, **E** stages I–II, **F** stages III–IV, **G** T1–2, **H** T3–4, **I** N0, **J** N123

Thereafter, we selected 12 types of immune cells with significantly different levels of infiltration in patients in the TCGA-HNSCC cohort, and explored the associations of these immune cells with 8 EMRGs. Most immune cells showed significantly different levels of infiltration between different groups, as revealed through the expression levels of the eight EMRGs (Fig. 8A–H). To observe the correlation between the 8-EMRG signature and six classical immune cells (B lymphocytes, CD4+ T lymphocytes, CD8+ T lymphocytes, macrophages, neutrophils, and myeloid dendritic cells), we determined the infiltration level of each immune cell in the TIMER database and performed Spearman's correlation analysis. We found a negative correlation between the infiltration of all six immune cells and the risk score, which accounted for the results of the low-risk group in GSEA and ESTIMATE analysis (Fig. 9I). Subsequently, we further analyzed relationships between eight EMRGs and immune cell infiltration (Fig. 9A–H). These results show that the activation of immune-related signaling pathways might increase the levels of immune cell infiltration in the low-risk group. Our 8-EMRG signature provides a potential strategy for predicting the levels of immune cell infiltration in the TIME.

3.6 Immune checkpoints and immune checkpoint inhibitor therapy in the 8-EMRG signature

To investigate the relationship between the benefits of immunotherapy and the 8-EMRG prognostic signature, we assessed differences in the expression levels of immune checkpoint genes between the two risk groups. Forty genes with significantly different expression levels were identified between the two risk groups, including 4 genes (*CD44, CD276, TNFSF9, NRP1*) that were upregulated in the high-risk group while the other 36 genes were downregulated (Fig. 10A). Thus, we speculate that low-risk patients may benefit more from immunotherapy. To verify the supposition, we input the

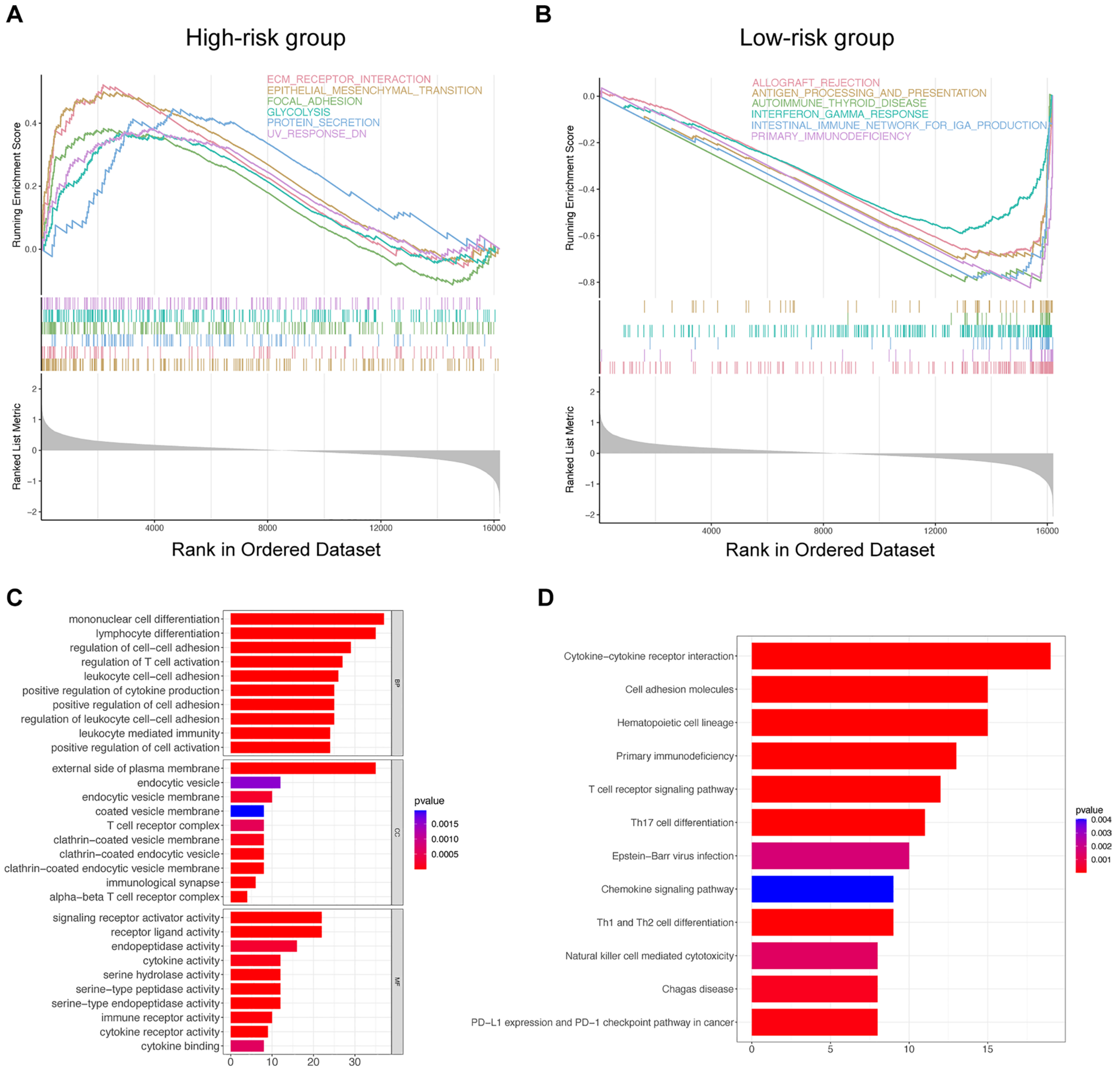

Fig. 6 Biological functional and pathway enrichment analysis of two risk groups based on the 8-EMRG signature. **A** GESA showing significant enrichment of cancer proliferation pathways in high-risk HNSCC patients. **B** GSEA showing significant enrichment of immune-related pathways in low-risk HNSCC patients. **C** GO analysis showing many immune-related biological processes were enriched. **D** KEGG analysis showing many immune-related pathways were enriched

expression profile (log2-normalized) in the TIDE website and acquired the response prediction score for each patient with HNSCC. The scores were positively correlated with the degree of response to immune checkpoint blockade. We observed that patients in the low-risk group presented lower response prediction scores, which revealed that immune checkpoint inhibitor therapy was more effective in the low-risk group (Fig. 10B). The prognostic signature was also considered an essential indicator to regulate drug sensitivity. We compared the half-maximal inhibitory concentration of chemotherapy drugs between the two risk groups to investigate the resistance potential of drugs in more detail. Among those, some representative drugs are displayed in Fig. 10C–L. Axitinib, cyclopamine, gefitinib, metformin, and methotrexate presented higher sensitivity in low-risk patients while cisplatin, docetaxel, imatinib, pazopanib, and vinorelbine presented higher sensitivity in high-risk patients, which may lead to new treatment options for patients with HNSCC.

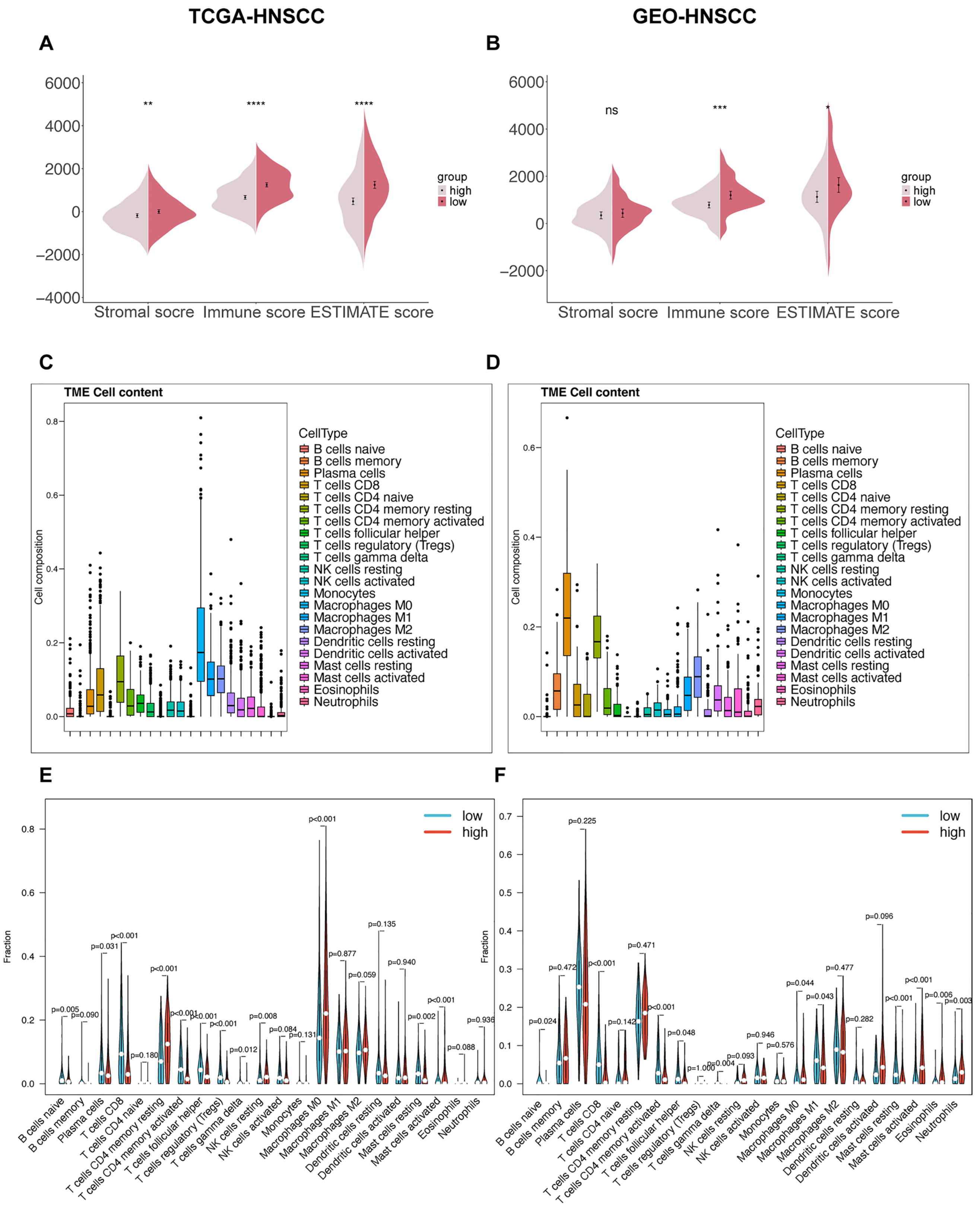

Fig. 7 Immune cell infiltration analyses between the high- and low-risk groups: the stromal, immune, and ESTIMATE scores between the high-risk and low-risk groups in TCGA patients (**A**) and GEO patients (**B**). The overall view of the relative proportions of 22 TIICs in TCGA patients (**C**) and GEO patients (**D**). The boxplots for the comparison of the 22 tumor-infiltrating immune cells between the high-risk (red) and low-risk groups (blue) in TCGA patients (**E**) and GEO patients (**F**)

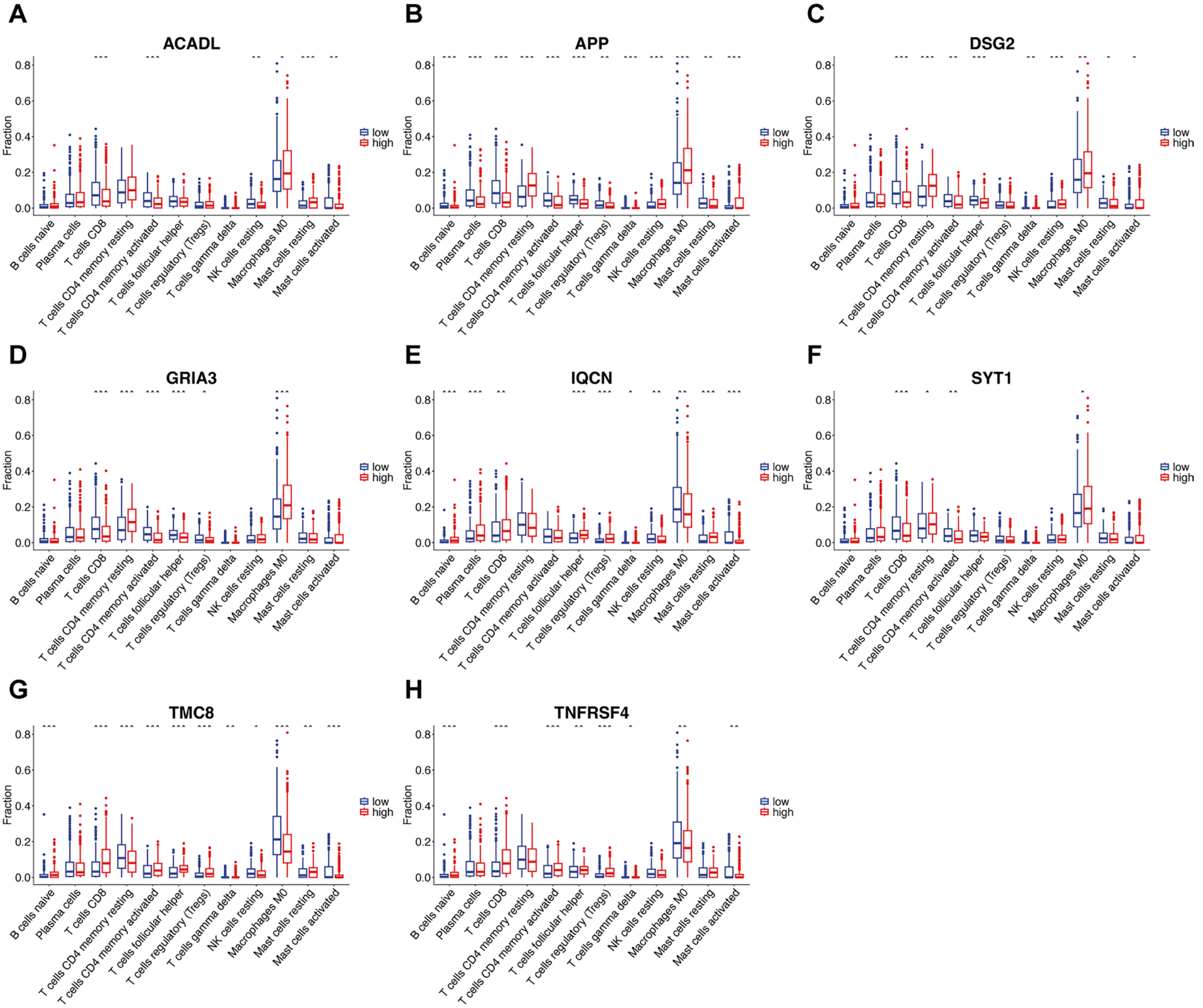

Fig. 8 Association of TIICs infiltration level with the 8 selected EMRGs: comparison of infiltration levels of 12 types of tumor-infiltrating immune cells according to *ACADL* (**A**), *APP* (**B**), *DSG2* (**C**), *GRIA3* (**D**), *IQCN* (**E**), *SYT1* (**F**), *TMC8* (**G**), and *TNFRSF4* (**H**) expression levels. *p < 0.05, **p < 0.01, and ***p < 0.001

3.7 Correlation between mutations in cancer-related genes and the 8-EMRG signatures'

To determine the role of the 8-EMRG signature in tumor mutation burden, we enumerated mutations in patients with HNSCC. Detailed information regarding mutations in each gene is shown in Fig. 11A, C. Missense mutations were the most commonly observed mutations in the two risk groups. Single nucleotide polymorphisms were more frequent than insertions or deletions. In addition, we found that C>T was the most common single nucleotide variant. The number of variants in each sample is shown in Fig. 11B, D. Our results indicate that tumor suppressor genes such as *TP53* (77% vs 63%) and *CDKN2 A* (22% vs 19%) presented higher mutation rates in high-risk patients than in low-risk patients.

3.8 Verification of the expression of 8 EMRGs between HNSCC tissues and tumor-adjacent normal tissue

We determined the mRNA levels of the 8 EMRGs in 5 pairs of HNSCC and tumor-adjacent normal tissue using qRT-PCR. The clinical characteristics of HNSCC samples for qRT-PCR is listed in Table S4. Our results (Fig. 12A) show that *SYT1* (P < 0.01), *IQCN* (P < 0.0001), and *ACADL* (P < 0.0001) were significantly downregulated in HNSCC tissues, whereas *TMC8* (P

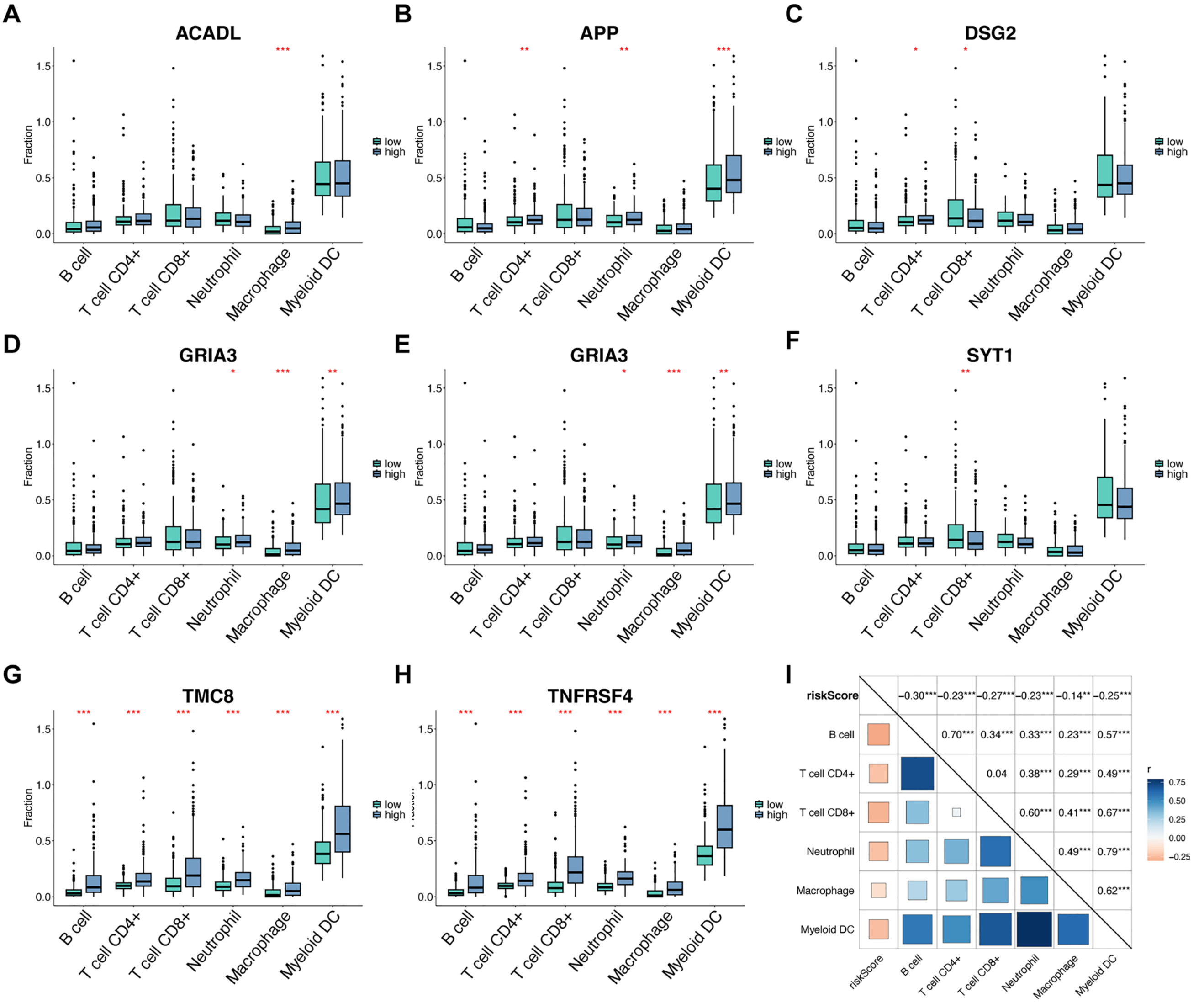

Fig. 9 Association of 6 immune cell infiltration levels with the 8 selected EMRGs: Comparison of infiltration levels of six immune cells according to the expression levels of *ACADL* (**A**), *APP* (**B**), *DSG2* (**C**), *GRIA3* (**D**), *IQCN* (**E**), *SYT1* (**F**), *TMC8* (**G**), and *TNFRSF4* (**H**). *p < 0.05, **p < 0.01, and ***p < 0.001. **I** The correlation between risk score and the infiltration levels of B cells, T cells CD4+, T cells CD8+, neutrophil, macrophage, and myeloid dendritic cells. Red presents negative correlation, blue presents positive correlation. *p < 0.05, **p < 0.01, ***p < 0.001. ns, No significance

< 0.0001), *DSG2* (P < 0.0001), and *APP* (P < 0.001) were significantly upregulated. In contrast, *TNFRSF4* and *GRIA3* expression levels did not differ significantly between the two groups.

To further illustrate differences in the expression levels of proteins encoded by the 8 EMRGs, we obtained representative images on immunohistochemical staining from the Human Protein Atlas (HPA, https://www.proteinatlas.org/). Our results show that the depth of staining was proportional to the expression levels of the proteins in tumor and normal tissues (Figure S1). HNSCC tissues presented high expression levels of *ACADL* and *DSG2* and low expression levels of *APP*. *GRIA3* and *TMC8* were expressed at equal levels in both HNSCC and normal tumor-adjacent tissues, yet *IQCN*, *SYT1*, and *TNFRSF4* displayed a negative staining pattern in both tissues. These results further validate the accuracy of our in silico analysis.

3.9 DSG2 promotes the proliferation and migration of tumor cells in HNSCC in vitro and in vivo

Numerous studies have reported that *DSG2* plays an important role in tumorigenicity in various cancers [22–24]; Interestingly, we performed GSEA based on the *DSG2*-related genes (|cor|> 0.2 and p < 0.05) and found that *DSG2* may

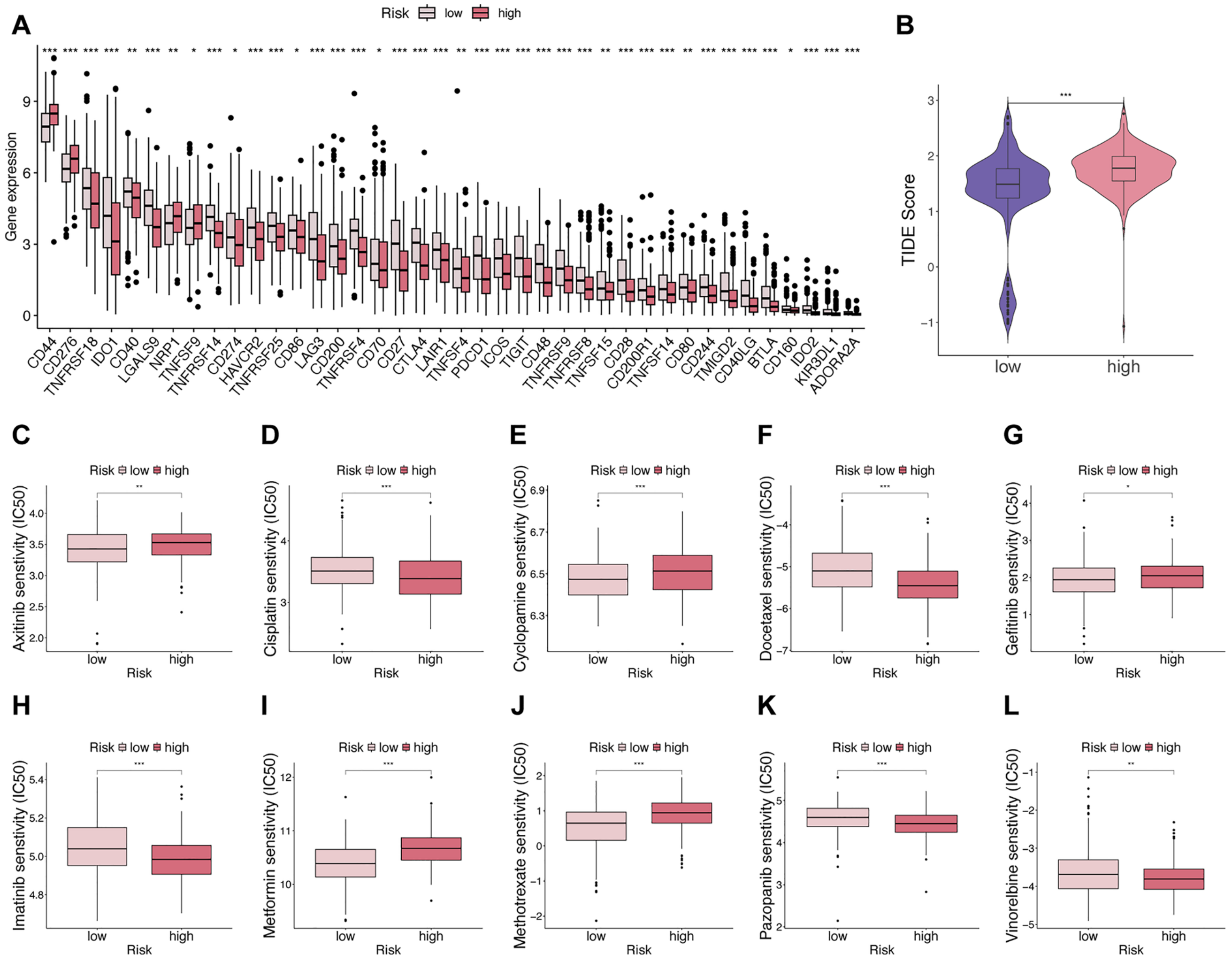

Fig. 10 Comparing the effects of immunotherapy and chemotherapy in the high- and low-risk groups. (A) The boxplots for the comparison of the immune checkpoint genes between the high-risk and low-risk groups in HNSCC patients. (B) The violin plot of the TIDE score in the high-risk and low-risk group. (C-L) Boxplot showing the differences in estimated IC50 values of 10 representative drugs (Axitinib, cisplatin, cyclopamine, docetaxel, gefitinib, imatinib, metformin, methotrexate, pazopanib, vinorelbine) between high-risk and low-risk groups. *$p < 0.05$, **$p < 0.01$, and ***$p < 0.001$

be involved in energy metabolism, such as GOBP_GLYCOSYLATION (NES = 1.56; p.adjust = 0.03), and REACTOME_GLUCOSE_METABOLISM (NES = 1.80; p.adjust = 0.02) (Figure S2 and Table S5). Furthermore, we found that the expression of *DSG2* was correlated with the infiltration level of 12 TIICs (Figure S3 A), and also found that the patients with higher *DSG2* expression exhibited lower immune scores and ESTIMATE scores (Figure S3B), which was consistent with the trend in our 8-EMRG signature, suggesting that *DSG2* may act as an immunosuppressive agent within TME. Hence, we next explored the function of *DSG2* in tumor cells in HNSCC. We silenced *DSG2* in FADU cells with lentiviral vectors harboring *DSG2*-specific shRNAs (*shDSG2*). Control cells were transfected with lentiviral vectors harboring negative control shRNA (*shNC*). As verified by qRT-PCR, the *shDSG2* we constructed down-regulated *DSG2* expression with an efficiency of 71.51% (Figure S4). Then, we assessed the effect of *DSG2* on cell proliferation by using the CCK-8 assay, and found that *DSG2* silencing reduced cell proliferation (Fig. 12B). Thereafter, we assessed the oncogenic potential of *DSG2* in vitro using the plate colony formation assay and found that *DSG2* knockdown reduced tumor growth in HNSCC (Fig. 12C). Furthermore, we assessed the effect of *DSG2* on cellular invasiveness using the Transwell chamber assay and found that *DSG2* silencing reduced the FADU cell invasiveness (Fig. 12D). To further demonstrate the effect of *DSG2* on tumorigenicity, we subcutaneously injected 10^5 parental FADU-*shNC* cells, FADU-*shDSG2#1* cells, and FADU-*shDSG2#2* cells into the left armpits of nude mice. We found that *DSG2* silencing resulted in the formation of smaller tumors (Fig. 12E, F).

Collectively, these results suggest that *DSG2* plays a pivotal oncogenic role in HNSCC in vitro and in vivo.

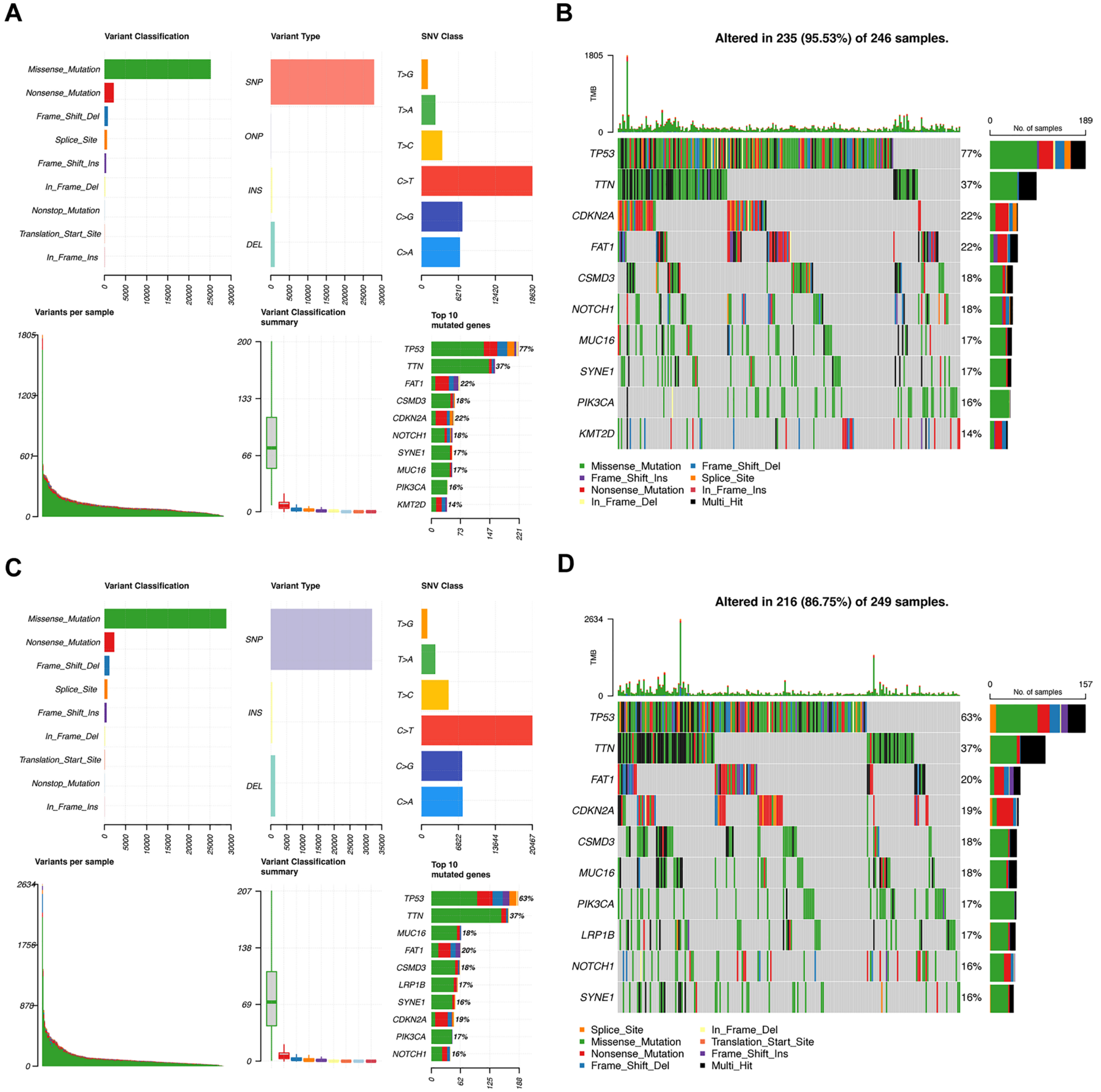

Fig. 11 Somatic mutation landscape in HNSCC patients. **A**–**D** The MAF-summary plots show the variant classification, variant types, SNV class, variants per sample, variant classification summary, and the top 10 mutated genes in the high-risk (**A**) and low-risk group (**C**). The oncoplots display the mutation profile of the top 10 frequently mutated types in the high-risk (**B**) and low-risk groups (**D**). Each column represents individual patients and mutated genes arranged by mutation rates. The right panel shows the mutation percentage, and color coding indicates the mutation type

4 Discussion

In our study, 877 EMRDEGs were identified from 502 HNSCC and 44 normal tissues in the TCGA-HNSCC cohort. A prognostic model was established, which integrated eight EMRGs including *ACADL*, *APP*, *DSG2*, *GRIA3*, *IQCN*, *SYT1*, *TMC8*, and *TNFRSF4*. Our study shows that the risk score can be used as an independent index for predicting survival among patients with HNSCC. The identified signature was integrated with clinical characteristics to generate the nomogram and calibration curve, which reliably confirmed accurate predictions of prognosis for patients with HNSCC. Based on the

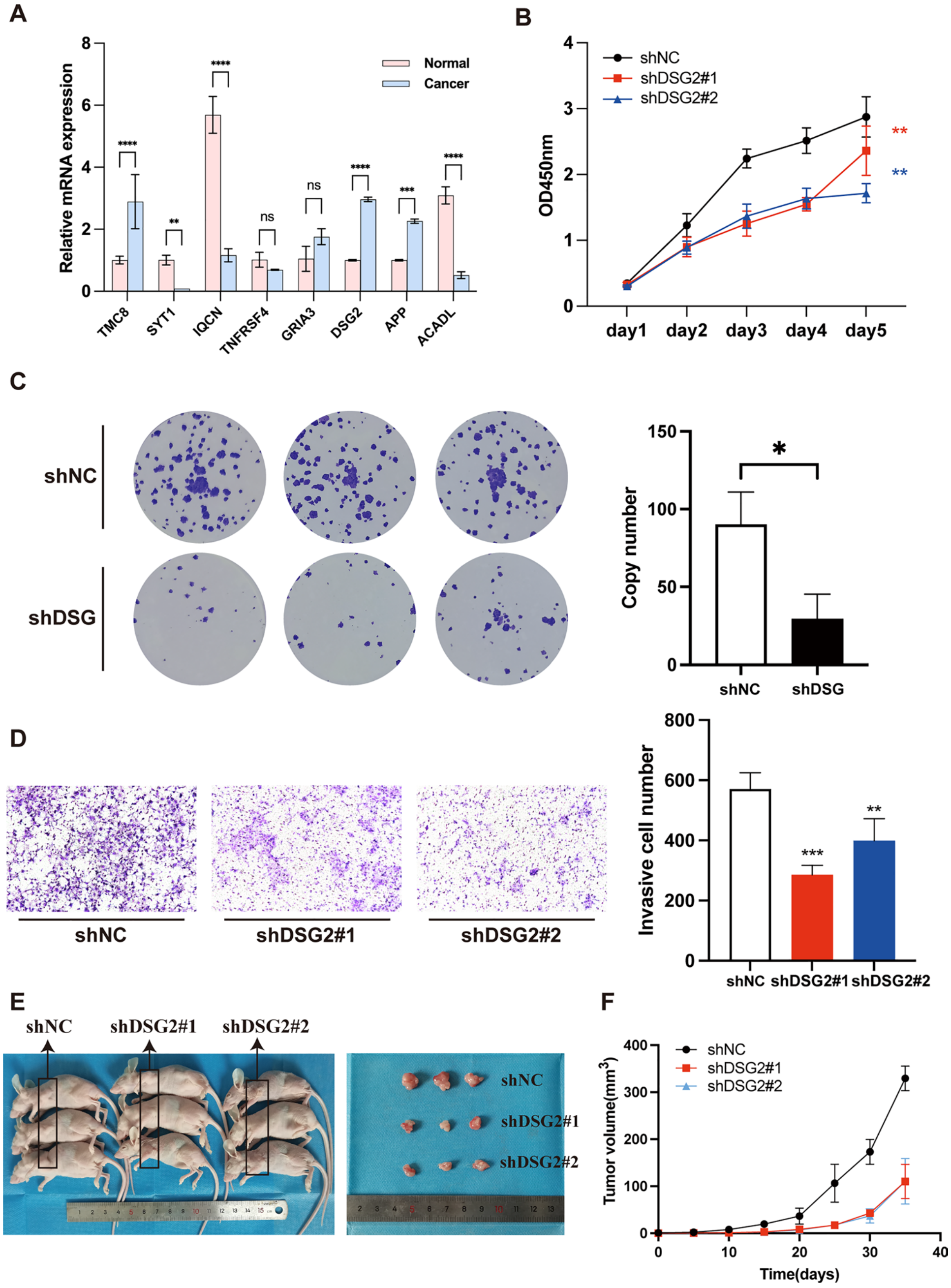

Fig. 12 *DSG2* promotes the tumorigenicity of HNSCC cells in vitro and in vivo. **A** The mRNA expression analysis by qRT−PCR. **B** Knockdown of *DSG2* significantly reduced cell proliferation by CCK8 assay in FADU. **C** Representative image of the plate colony formation assay implying that knockdown of *DSG2* reduced growth of FADU cell. **D** Representative images of the Transwell invasion assay implying that knockdown of *DSG2* reduce FADU cell invasion. **E** Imaging of mice (left) and xenograft tumors (right) showed that *DSG2* silencing led to smaller tumors. **F** Tumor formation growth curves. *$p < 0.05$, **$p < 0.01$, ***$p < 0.001$, ****$p < 0.0001$. ns, No significance

TCGA and GEO cohorts, Kaplan–Meier survival curves and ROC curves were plotted and their results show the robustness of the signature's prognostic power. GSEA was then conducted to interpret the molecular mechanism under the prognostic capability of the 8-EMRG signature. Higher risk scores represented more active tumor proliferation, while lower risk scores represent higher levels of immune cell infiltration. Furthermore, we performed ESTIMATE, CIBERSORT, and TIMER analyses to further determine the association between the signature and the TIME. Moreover, we found that immune checkpoint inhibitor therapy may be more effective in low-risk patients.

In particular, the correlation between key genes in the signature and the integration of energy metabolism has been investigated. For example, *ACADL*, *APP*, and *DSG2* were ascertained to participate in pathways related to the integration of energy metabolism [25–27], which verified the reliability of our gene model. Among them, *DSG2*, a transmembrane glycoprotein belonging to the desmosomal cadherin family, is critically involved in mediating intercellular junctions. While previous studies have established its pro-tumorigenic roles in cancers such as breast cancer and colon cancer [24, 28], conflicting evidence exists in other malignancies, including gallbladder and thyroid cancers [29, 30]. In this study, by performing GSEA, we found that *DSG2* may be involved in glycometabolism. Previous predictive studies have suggested an association between *DSG2* and tumor immune infiltration characteristics in pancreatic carcinoma [31]. Similarly, we found *DSG2* may be involved in immune regulation within the TME and, further, may act as an immunosuppressive agent. However, we have not yet experimentally validated this function. This issue requires further investigation in future research. Next, we explored the biological function of *DSG2* in HNSCC in vitro and in vivo, and found that *DSG2* silencing remarkably suppressed tumor cell proliferation and migration in HNSCC in vitro. Moreover, this effect was also observed in vivo. We concluded that *DSG2* can facilitate tumor progression, which is consistent with our signature defining *DSG2* as a risk gene. In addition, *ACADL*, having the highest positive correlation coefficient in the prognostic model, is a key enzyme catalyzing the first step in mitochondrial fatty acid oxidation and is an important source of energy [32]. Furthermore, *ACADL* was identified as a risk factor in esophageal squamous cell carcinoma while acting as a tumor suppressor in hepatocellular carcinoma, suggesting the paradoxical role of *ACADL* in different cancer types [33, 34]. As research on *ACADL* in HNSCC is inadequate, it is critical to explore the role and the potential mechanism of *ACADL* in HNSCC. In addition, the role of *GRIA3*, *IQCN*, *SYT1*, *TMC8*, and *TNFRSF4* in the integration of energy metabolism have also not yet been ascertained, and it is worth further exploring their roles in energy metabolism in HNSCC.

Furthermore, GSEA was performed to further evaluate the mechanism underlying the role of EMRGs in HNSCC progression. Six pathways were enriched in the high-risk group, three of which were cancer metastasis–related pathways (epithelial-mesenchymal transition [EMT], focal adhesion, and ECM-receptor interaction). As metastasis is still the major cause of cancer-related death, developing interventions targeting metastasis is a priority and EMT pathways seem to play a core role in metastasis [35]. The EMT is the process by which epithelial cells lose their integrity and become metastable—a critical step in immune evasion and cancer cell invasion [36]. Cells undergoing an EMT are associated closely with metabolic changes. Crosstalk occurs frequently between the EMT and energy metabolism; however, the potential mechanism and the principal underlying this crosstalk has been uncertain [37]. We observed that the EMT is involved in the interactions among the ECM, cytokines such as TNF-α and interleukin-6, and focal adhesion [38, 39]. It is worth investigating the multiple changes occurring during metabolic reprogramming during the EMT in HNSCC. Other pathways enriched in the high-risk group were glycolysis, protein secretion, and steroid hormone biosynthesis. The steroid hormone biosynthesis pathway has turned our sight into obesity-related host factor and cancer occurs. Steroid hormones affect tumor initiation, progression, and responses to therapy by changing the energy balance in some cancer types [40]. Development of the pharyngolaryngeal region differs between male and female individuals during evolution, and some tumors originating from this area contain hormone receptors, which—theoretically—makes them susceptible to hormone therapy. Enrichment of glycolysis and protein secretion pathways in the high-risk group both indicate the core event of cancer metabolic reprogramming, the Warburg effect, and amino acid metabolic reprogramming; they support cancer cell growth and provide energy by acting as metabolites and metabolic regulators [4]. Unexpectedly, the six main pathways enriched on GSEA in the low-risk group had correlations with immunity, including antigen processing, allograft rejection, antigen presentation, autoimmune thyroid disease, the interferon-γ response, primary immunodeficiency in the intestinal immune network with regard to immunoglobulin A production. Since the 8 prognostic genes and GSEA findings were strongly correlated with tumor immunity, we performed further analysis for the TIME.

Despite treatment with surgery, chemotherapy, and radiotherapy, the prognosis of patients with HNSCC remains very poor. In such cases, adjuvant immunotherapy may be helpful in treating malignant lesions and preventing disease recurrence. Extensive studies on the TIME have revealed the important role of TIICs in tumor spread, recurrence, metastasis, and immunotherapy responses, suggesting that the regulation of the TIME may provide strategies for targeted therapy of HNSCC. Some studies have also shown that the infiltration of tumor-infiltrating lymphocytes was positively correlated with OS, whereas M0 macrophages, neutrophils, and myeloid dendritic cells were negatively correlated with OS in the TIME in HNSCC [41, 42]. Furthermore, infiltration levels of antitumor immune cells such as activated memory CD4+ T lymphocytes, CD8+ T lymphocytes, plasma cells, follicular helper T lymphocytes, and γδ T lymphocytes were low in the high-risk group, and immunosuppressive cells such as M0 macrophages had higher infiltration levels. Interestingly, some studies reported that infiltration levels of regulatory T lymphocytes were positively correlated with OS in HNSCC, which is in line with our results [43–45]. In addition, we found associations between the eight EMRGs within the model and immunity in HNSCC. Interestingly, some studies reported that TNFRSF4 increased the proliferation and activation of effector T lymphocytes, which play a critical role in mechanisms underlying the contribution of regulatory T lymphocytes in outcomes of patients with HNSCC [46, 47]. Furthermore, *TMC8* exerts anti–human papillomavirus effects by regulating the infiltration of CD4+ T lymphocytes, which could serve as a potential prognostic marker [48–50]. Consequently, *TNFRSF4* and *TMC8* could represent potential targets for future therapeutics to control HNSCC progression. The remaining 6 genes within the model are not associated with the TIME in HNSCC, but our results show that they are of great research value in this field and could be further explored.

5 Conclusions

In summary, our study constructed an energy metabolism–related prognostic signature, which could be used to predict the survival prognosis of patients with HNSCC. Furthermore, we observed a correlation between the prognostic signature and tumor immune microenvironment and screened out some immune checkpoints and representative drugs, which could provide new targets to enhance the benefits of immunotherapy.

Acknowledgements We sincerely acknowledge The Cancer Genome Atlas (TCGA), UCSC Xena, and Gene Expression Omnibus database (GEO) for providing transcriptomic and clinicopathological data. We also acknowledge the Human Protein Atlas (https://www.proteinatlas.org/) for providing images of the IHC for our study.

Author contributions Z.K.Y and Y.B wrote the paper. C.Y.F and L.C.W designed research. L.C.W, G.L.S, and C.Y.F contributed to the research coordination. Z.K.Y and Y.B performed research. All authors reviewed the manuscript.

Funding This research was funded by the Natural Science Foundation of Hunan Province, Grant number no. 2023 JJ60064 and no. 2024 JJ9521.

Data availability The original contributions presented in the study are included in the article/Supplementary Material. The data regarding the integration of energy metabolism was downloaded from this article (https://linkinghub.elsevier.com/retrieve/pii/S2211-1247(18)30438-8), which was also listed in the Supplementary Material. The RNA-seq data can be found in the TCGA database with the project ID: TCGA-HNSC (https://portal.gdc.cancer.gov/projects/TCGA-HNSC), and the clinical information can be downloaded in UCSC Xena (https://xenabrowser.net/datapages/?cohort=GDC%20TCGA%20Head%20and%20Neck%20Cancer%20(HNSC)&removeHub=https%3A%2F%2Fxena.treehouse.gi.ucsc.edu%3A443). Gene expression data are available at GEO with the accession number: GSE41613, and GSE10300 (https://www.ncbi.nlm.nih.gov/geo/query/acc.cgi?acc=GSE41613, and https://www.ncbi.nlm.nih.gov/geo/query/acc.cgi?acc=GSE10300). The IHC images from the Human Protein Atlas are available from https://www.proteinatlas.org/ENSG00000115361-ACADL/cancer/head+and+neck+cancer, https://www.proteinatlas.org/ENSG00000142192-APP/cancer/head+and+neck+cancer, https://www.proteinatlas.org/ENSG00000046604-DSG2/cancer/head+and+neck+cancer, https://www.proteinatlas.org/ENSG00000125675-GRIA3/cancer/head+and+neck+cancer, https://www.proteinatlas.org/ENSG00000130518-IQCN/cancer/head+and+neck+cancer, https://www.proteinatlas.org/ENSG00000067715-SYT1/cancer/head+and+neck+cancer, https://www.proteinatlas.org/ENSG00000167895-TMC8/cancer/head+and+neck+cancer, and https://www.proteinatlas.org/ENSG00000186827-TNFRSF4/cancer/head+and+neck+cancer. The hyperlinks for the other database resources used in this article can be found in the Method section. Further inquiries can be directed to the corresponding authors.

Declarations

Ethics approval All procedures in our study involving human tissues and animals adhered to the ethical standards set by the Institutional Ethics Committee of The Fourth Hospital of Changsha, as well as the 1964 Helsinki Declaration and its subsequent amendments. The code for the animal study protocol was CSSDSYY-YXLL-SC-2023-03-03, while the code for the human study protocol was CSSDSYY-YXLL-SC-2023-03-163. Written informed consent was obtained from all patients.

Conflicts of interest The authors declare no competing interests.

Competing interests The authors declare no competing interests.

References

1. Jung K, et al. Squamous cell carcinoma of head and neck: what internists should know. Korean J Intern Med. 2020;35(5):1031–44.
2. Weiss J, Hayes DN. Classifying squamous cell carcinoma of the head and neck: prognosis, prediction and implications for therapy. Expert Rev Anticancer Ther. 2014;14(2):229–36.
3. Van den Bossche V, et al. Microenvironment-driven intratumoral heterogeneity in head and neck cancers: clinical challenges and opportunities for precision medicine. Drug Resist Updates. 2022;60: 100806.
4. Li Z, Zhang H. Reprogramming of glucose, fatty acid and amino acid metabolism for cancer progression. Cell Mol Life Sci. 2016;73(2):377–92.
5. Gillespie M, et al. The reactome pathway knowledgebase 2022. Nucleic Acids Res. 2022;50(D1):D687-d692.

6. Peng X, et al. Molecular characterization and clinical relevance of metabolic expression subtypes in human cancers. Cell Rep. 2018;23(1):255-269.e4.
7. Wang G, et al. Tumor microenvironment in head and neck squamous cell carcinoma: functions and regulatory mechanisms. Cancer Lett. 2021;507:55–69.
8. Xia L, et al. The cancer metabolic reprogramming and immune response. Mol Cancer. 2021;20(1):28.
9. Blum A, Wang P, Zenklusen JC. SnapShot: TCGA-analyzed tumors. Cell. 2018;173(2):530.
10. Goldman MJ, et al. Visualizing and interpreting cancer genomics data via the Xena platform. Nat Biotechnol. 2020;38(6):675–8.
11. Lohavanichbutr P, et al. A 13-gene signature prognostic of HPV-negative OSCC: discovery and external validation. Clin Cancer Res. 2013;19(5):1197–203.
12. Cohen EE, et al. A feed-forward loop involving protein kinase Calpha and microRNAs regulates tumor cell cycle. Cancer Res. 2009;69(1):65–74.
13. Ritchie ME, et al. Limma powers differential expression analyses for RNA-sequencing and microarray studies. Nucleic Acids Res. 2015;43(7): e47.
14. Kamarudin AN, Cox T, Kolamunnage-Dona R. Time-dependent ROC curve analysis in medical research: current methods and applications. BMC Med Res Methodol. 2017;17(1):53.
15. Wu, T., et al., clusterProfiler 4.0: A universal enrichment tool for interpreting omics data. Innovation (Camb), 2021. **2**(3): p. 100141.
16. Liberzon, A., et al., Molecular signatures database (MSigDB) 3.0. Bioinformatics, 2011. **27**(12): p. 1739–40.
17. Yoshihara K, et al. Inferring tumour purity and stromal and immune cell admixture from expression data. Nat Commun. 2013;4:2612.
18. Chen B, et al. Profiling tumor infiltrating immune cells with CIBERSORT. Methods Mol Biol. 2018;1711:243–59.
19. Li T, et al. TIMER: a web server for comprehensive analysis of tumor-infiltrating immune cells. Cancer Res. 2017;77(21):e108–10.
20. Jiang P, et al. Signatures of T cell dysfunction and exclusion predict cancer immunotherapy response. Nat Med. 2018;24(10):1550–8.
21. Geeleher P, Cox N, Huang RS. pRRophetic: an R package for prediction of clinical chemotherapeutic response from tumor gene expression levels. PLoS ONE. 2014;9(9): e107468.
22. Qin S, et al. DSG2 expression is correlated with poor prognosis and promotes early-stage cervical cancer. Cancer Cell Int. 2020;20:206.
23. Liu YQ, et al. Serine/threonine-protein kinase D2-mediated phosphorylation of DSG2 threonine 730 promotes esophageal squamous cell carcinoma progression. J Pathol. 2024;263(1):99–112.
24. Chang, P.H., et al., Interplay between desmoglein2 and hypoxia controls metastasis in breast cancer. Proc Natl Acad Sci U S A, 2021. **118**(3).
25. Myo Min KK, et al. Desmoglein-2 is important for islet function and β-cell survival. Cell Death Dis. 2022;13(10):911.
26. Chen Z, Zhong C. Decoding Alzheimer's disease from perturbed cerebral glucose metabolism: implications for diagnostic and therapeutic strategies. Prog Neurobiol. 2013;108:21–43.
27. Suzuki S, et al. Cold temperature blocks thyroid hormone-induced changes in lipid and energy metabolism in the liver of Lithobates catesbeianus tadpoles. Cell Biosci. 2016;6:19.
28. Kamekura R, et al. Loss of the desmosomal cadherin desmoglein-2 suppresses colon cancer cell proliferation through EGFR signaling. Oncogene. 2014;33(36):4531–6.
29. Lee SH, et al. Loss of desmoglein-2 promotes gallbladder carcinoma progression and resistance to EGFR-targeted therapy through Src kinase activation. Cell Death Differ. 2021;28(3):968–84.
30. Lee K, et al. Dsg2-mediated c-Met activation in anaplastic thyroid cancer motility and invasion. Endocr Relat Cancer. 2020;27(11):601–14.
31. Tang P, et al. Identifying and Validating an Acidosis-Related Signature Associated with Prognosis and Tumor Immune Infiltration Characteristics in Pancreatic Carcinoma. J Immunol Res. 2021;2021:3821055.
32. Zhao X, et al. ACADL plays a tumor-suppressor role by targeting Hippo/YAP signaling in hepatocellular carcinoma. NPJ Precis Oncol. 2020;4:7.
33. Sun YL, et al. A prognostic model based on six metabolism-related genes in colorectal cancer. Biomed Res Int. 2020;2020:5974350.
34. Yu DL, et al. Acyl-CoA dehydrogenase long chain expression is associated with esophageal squamous cell carcinoma progression and poor prognosis. Onco Targets Ther. 2018;11:7643–53.
35. Majidpoor J, Mortezaee K. Steps in metastasis: an updated review. Med Oncol. 2021;38(1):3.
36. Hua W, et al. TGFβ-induced metabolic reprogramming during epithelial-to-mesenchymal transition in cancer. Cell Mol Life Sci. 2020;77(11):2103–23.
37. Jia D, et al. Towards decoding the coupled decision-making of metabolism and epithelial-to-mesenchymal transition in cancer. Br J Cancer. 2021;124(12):1902–11.
38. Yang K, et al. Homeostatic control of metabolic and functional fitness of T(reg) cells by LKB1 signalling. Nature. 2017;548(7669):602–6.
39. Badeaux MD, et al. Arginase therapy combines effectively with immune checkpoint blockade or agonist anti-OX40 immunotherapy to control tumor growth. Cancer Immunol Res. 2021;9(4):415–29.
40. Hursting SD, et al. Obesity, energy balance, and cancer: new opportunities for prevention. Cancer Prev Res. 2012;5(11):1260–72.
41. Johnson DE, et al. Head and neck squamous cell carcinoma. Nat Rev Dis Primers. 2020;6(1):92.
42. Peltanova B, Raudenska M, Masarik M. Effect of tumor microenvironment on pathogenesis of the head and neck squamous cell carcinoma: a systematic review. Mol Cancer. 2019;18(1):63.
43. Russell S, et al. Immune cell infiltration patterns and survival in head and neck squamous cell carcinoma. Head Neck Oncol. 2013;5(3):24.
44. Ferris RL. Immunology and immunotherapy of head and neck cancer. J Clin Oncol. 2015;33(29):3293–304.
45. Mandal R, et al. The head and neck cancer immune landscape and its immunotherapeutic implications. JCI Insight. 2016;1(17): e89829.
46. Qi, Z., et al., Single-Cell Deconvolution of Head and Neck Squamous Cell Carcinoma. Cancers (Basel), 2021. **13**(6).
47. So T, Ishii N. The TNF-TNFR family of co-signal molecules. Adv Exp Med Biol. 2019;1189:53–84.
48. Imahorn E, et al. Novel TMC8 splice site mutation in epidermodysplasia verruciformis and review of HPV infections in patients with the disease. J Eur Acad Dermatol Venereol. 2017;31(10):1722–6.
49. Liang C, et al. A coding variant in TMC8 (EVER2) is associated with high risk HPV infection and head and neck cancer risk. PLoS ONE. 2015;10(4): e0123716.

50. Lin B, et al. Comprehensive co-expression analysis reveals TMC8 as a prognostic immune-associated gene in head and neck squamous cancer. Oncol Lett. 2021;22(1):498.